American Society of Mechanical Engineers

ASME Accepted Manuscript Repository

Institutional Repository Cover Sheet

Richard John   Jefferson-Loveday

First   *Last*

ASME Paper Title: Differential Equation-based Specification of Turbulence Integral Length Scales for Cavity Flows

Authors: Richard John Jefferson-Loveday

ASME Journal Title: Journal of Engineering for Gas Turbines and Power

Volume/Issue   _____   Date of Publication (VOR* Online)   _____

ASME Digital Collection URL: _____

DOI: _____

*VOR (version of record)

Differential Equation-based Specification of Turbulence Integral Length Scales for Cavity Flows

Richard J. Jefferson-Loveday

Gas Turbines and Transmissions Research Centre

Faculty of Engineering

The University of Nottingham, UK

Email: Richard.Jefferson-Loveday@nottingham.ac.uk

ABSTRACT

A new modeling approach has been developed that explicitly accounts for expected turbulent eddy length scales in cavity zones. It uses a hybrid approach with Poisson and Hamilton-Jacobi differential equations. These are used to set turbulent length scales to sensible expected values. For complex rim-seal and shroud cavity designs, the method sets an expected length scale based on local cavity width which accurately accounts for the large-scale wake-like flow structures that have been observed in these zones. The method is used to generate length scale fields for three complex rim-seal geometries. Good convergence properties are found and a smooth transition of length scale between zones is observed. The approach is integrated with the popular Menter-SST RANS turbulence model and reduces to the standard Menter model in the mainstream flow. For validation of the model, a transonic deep cavity simulation is performed. Overall the Poisson-Hamilton-Jacobi model shows significant quantitative and qualitative improvement over the standard Menter and $k - \varepsilon$ two-equation turbulence models. In some instances it is comparable or more accurate than high-fidelity LES. In its current development, the approach has been extended through the use of an initial stage of length scale estimation using a Poisson equation. This essentially reduces the need for user objectivity. A key aspect of the approach is that the length scale is automatically set by the model. Notably, the current method is readily implementable in an unstructured, parallel processing computational framework.

NOMENCLATURE

C, CD cross-diffusion terms

D turbulence diffusion term

E total energy

f forcing function

G turbulence generation term

H shape factor

k turbulent kinetic energy or thermal conductivity

ℓ mixing length

L cavity length or Poisson turbulence length scale

$\tilde{L}$ turbulence length scale

$\tilde{L}_{PHJ}$ Poisson-Hamilton-Jacobi turbulence length scale

Ma Mach number

N exponent in blending function

p static pressure

Pr Prandtl number

q heat flux

Q solution vector

R residual vector

Re   Reynolds number

S_{ij} strain rate tensor

t time

$\tilde{t}$ pseudo-time

T temperature

T_i freestream turbulence intensity

u_i velocity components in x_i direction

u_τ friction velocity

U freestream velocity

U   pseudo-velocity vector

x_i Cartesian space coordinate, $i = 1, 2, 3$

y nearest (normal) wall distance or spatial coordinate

y^+ wall-normal non-dimensional wall unit

Y turbulence destruction term

α_f filter parameter

β residual smoothing factor

Γ	diffusion analogous coefficient
δ	boundary layer thickness
δ_{ij}	Kronecker delta
$\tilde{\varepsilon}$	constant in diffusion analogous coefficient evaluation
ε	dissipation rate of turbulence energy
η	blending function
θ	momentum thickness
κ	Von Karman constant
μ	dynamic viscosity
μ_T	turbulent dynamic viscosity
ρ	density
σ	blending function
τ_{ij}	stress tensor
ϕ	Poisson variable
ω	specific turbulence dissipation rate
Ω	vorticity

1 Introduction

In order to accurately simulate turbomachinery flows it is often necessary to include the effects of real engine geometry features such as rim-seals and shroud cavities. When performing design based calculations involving an optimization procedure, it is typical to run many thousands of iterative simulations. Hence it is not currently feasible within the industrial environment to run fully unsteady calculations, especially when there are multiple cavities and stages included. It is well known that secondary geometries (e.g. rim seals and labyrinth seals) can significantly alter the blockage and loss distributions in the primary flow of turbines and compressors which can in turn lower the effectiveness and efficiency of a turbomachine from anticipated levels. Experience has shown the importance of including the effects of cavities in CFD calculations [1] [2] [3] where fine grids are required to model more complex features. In some cases, cavity meshes can contain as many grid nodes as the primary geometry itself, and if low velocities are encountered, this can lead to long run times, especially in unsteady simulations. Hence it is common in the early-to-mid design stage to run comparatively low-order steady calculations, particularly for optimization studies where many thousands of geometries/configurations are tested. Inspired by this need, Gangwar [4] and Lukovic [5] explored deterministic stress modeling of idealized cavity flows. Lukovic used URANS simulations as training data for a neural network source model. In this case, the neural network was used as a form of interpolator in the design space. Global performance (cavity drag) prediction was found to be predicted within around 10% of the URANS at two orders of magnitude lower cost. Further work on the application of neural networks to cavity flows can be found in Gangwar [6], Lukovic et al. [7], Lukovic et al. [8] and Lukovic et al. [9] (this work includes a wall tangential velocity component which brings greater realism to aero-engine rim-seal flows).

The model here is an extension to a previously developed model to improve cavity modeling. In [10], a novel differential equation approach was used to set turbulence length scales in separated large-scale (wake) flow regimes (such as those encountered in cavities) based on traditional expected length scales. In these flows large scale vortices are shed from corners and sharp edges and the wall distance is an inappropriate length scale. Even more advanced two-equation RANS models were found to encounter problems when dealing with these flows. In gas turbines, convecting wake flows are commonly found in shroud regions, hub cavities, endwall flows, internal turbine blade cooling passages and cutback trailing edge zones [10]. The approach was validated for canonical flow test cases and demonstrated significant improvement compared with popular two equation RANS models. For a high Reynolds number cylinder flow, the re-attachment length error improved by 180% and for a cavity flow, the drag coefficient error by 30%. The model also enabled converged solutions to be obtained in such highly unsteady flow regimes. Out of ten widely used RANS models tested, only two would converge to a steady point.

In its current development, the approach has been extended through the use of an initial stage of length scale estimation using a Poisson equation. This essentially reduces the need for user objectivity because the length scale is automatically set by the model and not by the modeler. The length scales are blended with classical turbulence scales through injection into the boundary conditions of a Hamilton-Jacobi equation solution. The approach is called the Poisson-Hamilton-Jacobi approach (PHJ) and is readily applicable to unstructured flow solvers, providing a natural and elegant way to impose integral wake scales in detached flow zones whilst preserving accurate modeling of near-wall scales on attached boundary layers.

2 Poisson-Hamilton-Jacobi Length Scale

A modified length scale (which is based on expected turbulence length-scales in problem zone areas of gas turbines such as shroud cavities and rim-seals) model is presented. It is a pragmatic approach which is implemented through the use of a hybrid Hamilton-Jacobi/Poisson differential equation approach for a turbulent length-scale. This provides accurate near-wall distances but appropriate wake scales away from walls (and within cavities) and a smooth blending between zones. The desired integral scale is simply enforced via a Dirichlet boundary condition which is informed via a precursor Poisson equation solution.

An exact equation for a near surface turbulence length scale of $\ell = \kappa d$ (where $\kappa = 0.41$ is the von Karman constant) that can be readily derived using simple coordinate geometry is the hyperbolic eikonal equation [10] defined as:

$$|\nabla \tilde{L}| = 1 + \Gamma \nabla^2 \tilde{L} \tag{1}$$

where $\tilde{L}\ (= \ell/\kappa = d)$ is a turbulence length scale and Γ is a diffusion analogous coefficient. The equation models a front propagating at unit velocity from surfaces. In fact, $\tilde{L}$ is actually the first arrival time of the front. If the velocity is equal to unity this time is equivalent to wall distance. If $\Gamma = f(\tilde{L})$, the front velocity is modified and the resulting Hamilton-Jacobi

(HJ) equation will also give additional useful traits as outlined in [11] and [12]. Here:

$$\Gamma = \tilde{\varepsilon}\tilde{L} \tag{2}$$

where $\tilde{\varepsilon}$ is a constant. Finite values of $\tilde{\varepsilon}$ can improve stability which is useful for securing rapid iterative convergence, here a value of 0.4 is used. Defining a pseudo-velocity vector $\mathbf{U} = \nabla\tilde{L}$ Equation (1) can be re-expressed as:

$$\mathbf{U} \bullet \nabla\tilde{L} = 1 + \Gamma\nabla^2\tilde{L} \tag{3}$$

and for consistency with the CFD solver, Equation (3) is re-expressed with a convective type LHS term written in the mathematically identical, conservation form below:

$$\nabla \bullet (\tilde{L}\mathbf{U}) = 1 + \Gamma\nabla^2\tilde{L} \tag{4}$$

where the boundary conditions for the standard turbulence length scale are $\tilde{L} = 0$ at wall boundaries and $\partial\tilde{L}/\partial\mathbf{n}$ at all other boundaries.

Setting $\mathbf{U} = 0$ & $\Gamma = 1$, Equation (4) reduces to a Poisson equation of the following form:

$$\nabla^2\phi = -1 \tag{5}$$

The equation is similar to that for temperature within a uniformly conducting medium, having a uniform heat source, and in contact with solids and other surfaces at which the temperature is held at zero. The variable ϕ is not itself a length scale, even though it is proportional to wall distance very close to a wall. It has units of length-squared and as such has no physical basis [13]. However, a turbulence length scale $\tilde{L}$ can be derived by considering a simple geometry between two parallel walls assumed infinite in the wall-parallel direction and it has been found to give plausible results in extreme departures from this [13]. Through integration of Equation (5), and substitution of appropriate boundary conditions, it can related to ϕ through the following auxiliary relationship:

$$L_{min,max} = \pm\sqrt{\sum_{j=1,3}\left(\frac{\partial\phi}{\partial x_j}\right)^2} + \sqrt{\sum_{j=1,3}\left(\frac{\partial\phi}{\partial x_j}\right)^2 + 2\phi} \tag{6}$$

The analytical derivation of (6) is given in [14]. The minimum absolute root of the equation corresponds to the nearest wall distance (y) and the maximum absolute root the furthest wall distance. At boundaries, the sum of the two roots will give the local cavity width. Since the cavity size limits the maximum turbulent eddy size the sum of the two roots can be used to automatically fix a plausible turbulence length scale for the large turbulent eddies (the integral scales). This is used as a Dirichlet boundary condition for solution of the Hamilton-Jacobi Equation (4). Equation (4) will give accurate wall distances outside the cavity and automatically elevated distances in the cavity zone. The Laplacian in Equation (4) blends the distinctly different length scales.

Figure 1 illustrates the process chain. First an initial run of the geometry of interest is performed to solve the Poisson equation (5). This provides a local cavity length scale equal to the local cavity width. Next the Hamilton-Jacobi Equation (4) is solved with the maximum Poisson equation root simply enforced via a Dirichlet boundary condition. The approach provides a natural and elegant way to impose integral wake scales in detached flow zones within a single process for the design engineer. In this paper the Poisson-Hamilton-Jacobi method is examined with reference to rim seal configurations, although the model has potential for many other engine areas including shroud cavities and turbine blade cooling passages.

3 Solvers and Numerics

The standard Menter SST and Poisson-Hamilton-Jacobi Menter SST approaches are performed using the in-house multi-block solver 'DOLPHIN'. This is a new code and has been written by the current author. It has been extensively validated using canonical flow test-cases. For spatial discretization a finite difference approach is used motivated by the relative ease of extension to higher order accuracy. The convective spatial derivative is calculated through solving a system of tri-diagonal equations:

$$\alpha\phi'_{i-1} + \phi'_i + \alpha\phi'_{i+1} = b\frac{\phi_{i+2} - \phi_{i-2}}{4\delta x} + a\frac{\phi_{i+1} - \phi_{i-1}}{2\delta x} \tag{7}$$

For the current simulations $\alpha = 0$, $a = 1$ and $b = 0$ giving an explicit second order central scheme. For stability, a filtering scheme is employed following Visbal [15]. The filter replaces the updated value of ϕ (the conserved variable) with a filtered variable $\hat{\phi}$ through the following equation:

$$\alpha_f\hat{\phi}_{i-1} + \hat{\phi}_i + \alpha_f\hat{\phi}_{i+1} = \sum_{n=0}^{N}\frac{a_n}{2}(\phi_{i+n} + \phi_{i-n}) \tag{8}$$

where $a_0, a_1, ...a_N$ are coefficients given in Table 1 and α_f is an adjustable parameter ($-0.5 < \alpha_f \leq 0.5$) where higher values of α_f correspond to a less dissipative filter. For the present simulations, $\alpha_f = 0.495$ and the order of accuracy is four. To maintain the scheme's order near boundaries, high-order one-sided formulae are used. For the first interior node:

$$\alpha_f \hat{\phi}_1 + \hat{\phi}_2 + \alpha_f \hat{\phi}_3 = a\phi_1 + b\phi_2 + c\phi_3 + d\phi_4 + e\phi_5 \tag{9}$$

where subscript '1' refers to a boundary node and subscript '2' refers to the first interior node etc. The coefficients for the fourth order filter at the first interior node are given in Table 2.

For viscous terms standard second order central differences are used. The governing equations are re-arranged as:

$$\frac{\partial Q}{\partial \tilde{t}} = R(Q) \tag{10}$$

and integrated in pseudo-time $\tilde{t}$ to a steady-state using a four stage Runge-Kutta scheme. Here Q is the solution vector. For the $(i,j,k)^{th}$ cell at the nth time step:

$$
\begin{aligned}
Q^1 &= Q^n + \frac{\Delta \tilde{t}}{2} R^n, \\
Q^2 &= Q^n + \frac{\Delta \tilde{t}}{2} R^1, \\
Q^3 &= Q^n + \Delta \tilde{t} R^2, \\
Q^{n+1} &= Q^n + \frac{\Delta \tilde{t}}{6} (R^n + 2R^1 + 2R^2 + R^3).
\end{aligned}
\tag{11}
$$

To accelerate convergence implicit residual averaging (or smoothing) is used as well as a multigrid approach. The former consists of the replacement of the residual, R, for a cell with an implicitly-averaged residual, $\tilde{R}$, where $\tilde{R}$ is the solution to the following:

$$(1 - \beta_y \Delta_{yy})(1 - \beta_z \Delta_{zz})(1 - \beta_x \Delta_{xx})\tilde{R} = R \tag{12}$$

Here Δ_{yy}, Δ_{zz}, Δ_{xx} are undivided second-difference operators and β_y, β_z, β_x are smoothing factors. For the current work smoothing factor values of $\beta_x = 1.0$ and $\beta_y = 1.0$ were used and the smoothing was applied at the end of every fourth stage.

A geometric multigrid strategy is also used as a convergence acceleration technique. In this work, a standard 'V-cycle' multigrid algorithm is utilized. Each coarse grid iteration uses a forcing function derived from information obtained on finer grid solutions. When the coarsest level has been reached, a series of interpolation steps transfer the corrections to progressively finer meshes and the cycle can begin again. For a fine mesh (h) and a coarse mesh ($2h$) the forcing function is

defined by:

$$f_{2h} = I_h^{2h} R_h - R_{2h}(Q_{2h}^{(0)})$$

(13)

where I_h^{2h} is the restriction operator and $R_{2h}(Q_{2h}^{(0)})$ is the coarse grid residual computed based on the restricted solution. It is introduced to the solution process as follows:

$$\frac{\partial}{\partial \tilde{t}} Q_{2h} = -[R_{2h}(Q_{2h}) + f_{2h}]$$

(14)

Upon completion at the coarsest mesh level, the corrections to the variables are prolongated back to the finer meshes using linear interpolation. For evaluation of the $k - \varepsilon$ model the commercial CFD solver Fluent version 15.0 is used. The solution of the governing equations uses the implicit density based solver with algebraic multigrid and a second order upwind Roe scheme. Turbulence closure uses the standard $k - \varepsilon$ model and enhanced wall functions. Full details of the numerical schemes can be found in [16].

4   Turbulence Model

The Poisson-Hamilton-Jacobi approach is applied to the popular Menter shear-stress transport (MSST) [17] RANS turbulence model. It is considered to be one of the most accurate two equation models for aerodynamic flows [18] and is widely used in industry. To enable a direct input of turbulence length scale, the Menter model destruction term is recast in cavity zones. The approach is similar to that of the MSST-DES method of Strelets et al. [19].

This two equation model solves for turbulent kinetic energy (k) and specific dissipation rate (ω). The standard transport equations are as follows:

$$\frac{Dk}{Dt} = \frac{\partial}{\partial x_i} \left[(\nu + \sigma_k \nu_T) \frac{\partial k}{\partial x_i} \right] + G^k - Y^k$$

(15)

$$\frac{D\omega}{Dt} = \frac{\partial}{\partial x_i} \left[(\nu + \sigma_\omega \nu_T) \frac{\partial \omega}{\partial x_i} \right] + G^\omega - Y^\omega + C^\omega$$

(16)

where the terms of the equations are given in Table 3.

Constants are calculated through a blending of the $k - \varepsilon$ and $k - \omega$ model constants using $\alpha = \alpha_1 F_1 + \alpha_2 (1 - F_1)$ etc.

and standard values are used [17].

The length scale of the model in terms of k and ω reads:

$$\tilde{L}_{MEN} = \frac{k^{1/2}}{\beta^*\omega} \tag{17}$$

where $\beta^* = 0.09$. For the Poisson-Hamilton-Jacobi method, the destruction term of the k transport equation is re-expressed to contain a length scale:

$$Y^k_{PHJ} = k^{3/2}/L \tag{18}$$

To blend between the cavity length scales ($\tilde{L}_{PHJ}$) and the mainstream length scales ($\tilde{L}_{MEN}$) the following function is used:

$$L = (1-\sigma)\tilde{L}_{PHJ} + \sigma\tilde{L}_{MEN} \tag{19}$$

Here, $\tilde{L}_{PHJ} = \tilde{L}$ and is obtained through the solution of Equation (4). The function σ is a blending function based on the ratio of the standard wall distance (y) and the Poisson-Hamilton-Jacobi length scale (L_{PHJ}) and is defined by:

$$\sigma = tanh\left(C\left(\frac{y}{\tilde{L}_{PHJ}}\right)^N\right) \tag{20}$$

The parameters C and N control the blending between the cavity and mainstream zones and here $C = N = 6$. The resulting length scale field was not particularly sensitive to values greater than this. In the mainstream zone $L = \tilde{L}_{MEN}$ and the standard model is recovered. In the cavity zone the destruction term is expressed in terms of the Poisson-Hamilton-Jacobi length scale $\tilde{L}_{PHJ}$.

4.1 Near-wall treatment

Wake type flow structures can be generated through a combination of factors including cavity shear-layer excitation through convective and acoustic waves [20] and/or shedding from sharp geometrical features such as seal tooth tips [10] [21]. For cases where there will be significant swirl, the dominant flow direction will be in the tangential direction and a formation of a boundary layer. Following Spalart [22], a function is used noting that in the log-law region of a boundary layer $\Omega = u_\tau/(\kappa y)$ and $\nu_T = u_\tau\kappa y$. Equivalently the function $\nu_T/(\Omega\kappa^2 y^2)$ will equal unity in a log law layer and decrease in the outer region. Using this the present work defines an additional blending function for the definition of a near-wall "damped"

length scale:

$$\tilde{L}_{PHJD} = (1-\eta)\tilde{L}_{PHJ} + \eta\tilde{L}_{MEN} \qquad (21)$$

where $\eta = min\{(\nu_T/\Omega\kappa^2 y^2)^6; 1.0\}$ and is raised to a power to decay rapidly in the outer layer. Equation (19) is modified to give:

$$L = (1-\sigma)\tilde{L}_{PHJD} + \sigma\tilde{L}_{MEN} \qquad (22)$$

and provides the local length scale input L for Equation (18).

5 Assessment of the Poisson-Hamilton-Jacobi Length Scale

To assess the Poisson-Hamilton-Jacobi method it is tested on three rim-seal configurations. Figure 2 shows the multi-block meshes used for, (a) a simple axial seal, (b) a seal with a single radial clearance, and (c) a seal with two radial clearances. Figure 3 shows nearest wall distance (y) and Poisson-Hamilton-Jacobi generated turbulent length scale contours ($\tilde{L}_{PHJ}$) for the different rim-seals. As can be seen the seals are increasing in complexity and have been designed to contain a wide range of spatial scales. Here, the L_{max} Dirichlet boundary condition is enforced below the hub line and a cut-off limit is applied corresponding to the maximum cavity width. Differential boundary conditions are applied ($\tilde{L}_{PHJ} = 0$ at walls and $\partial\tilde{L}_{PHJ}/\partial\mathbf{n}$ at all other boundaries) in a first order fashion. Initialization is such that $\tilde{L}_{PHJ} = \tilde{L}_i$ where $\tilde{L}_i$ is a length scale that is greater than the maximum cavity dimension. For all cases, there is a smooth transition of $\tilde{L}_{PHJ}$ between the main gas path and cavity. The injection of the Poisson generated length scale (which is based on the local cavity width) provides local HJ length scale fields and a smooth transition is observed between the different cavity zones.

6 Assessment For a Deep Cavity Flow

Detailed measurements using laser Doppler anemometry (LDA) for a deep cavity flow have been made by Forrestier and co-workers [23] at a Mach number of $Ma = 0.8$ and Reynolds Number (based on cavity length) of $Re = 860000$. The experiments were performed in a continuous wind tunnel with a constant cross-sectional area of $0.1 \times 0.12m^2$ area. Dry atmospheric air was supplied to the tunnel with an ambient pressure and temperature of $0.98 \times 10^5 Pa$ and $293K$ respectively. The cavity was located on the channel floor and spanned the whole width of the test section. The aspect ratios of length to depth (L/D) and depth to width (D/W) were 0.42 and 1 respectively. Boundary-layer transition was triggered well upstream of the cavity. A schematic of the simulation setup is shown in Figure 4. The freestream velocity is $U = 258m/s$, the length of the cavity is $L = 0.05$ m and the depth of the cavity is $D = 0.12$ m. The boundary layer at the inlet is defined using a shape factor and momentum thickness that were measured experimentally. The values are 1.3 and 0.65 mm respectively and the

experimentally measured turbulence intensity is 1.5% of the freestream velocity. The boundary layer at the inlet is defined using the following power-law profile:

$$\frac{\bar{u}}{U} = \left(\frac{y}{\delta}\right)^{\frac{1}{n}} \tag{23}$$

Here $n = 2/(H-1)$ where H is the shape factor ($H = 1.3$) and δ is obtained using:

$$\delta = \frac{\theta(n+1)(n+2)}{n} \tag{24}$$

where θ is the momentum thickness ($\theta = 0.65$ mm). The inlet turbulent kinetic energy is calculated as $k = 3/2(UT_i)^2$ and the specific dissipation rate at the inlet is $\omega = k^{1/2}/C_\mu^{1/4}\ell$ where $\ell = \kappa\delta$. Following Menter [24], ω is limited to a lower value of $10U/L$. If reached, the eddy viscosity is calculated as $\nu_T = \sqrt{3/2}UT_i\ell$ and k is obtained from the standard relationship $\nu_T = k/\omega$.

At the outlet, all flow variables are extrapolated using second order differences apart from the static pressure which is specified. At the inlet, the velocity, temperature and turbulent flow quantities are specified and the pressure is extrapolated from interior nodes. Towards the the upper wall, the mesh is rapidly expanded and a slip wall boundary condition is used. At the lower walls, a no-slip wall boundary condition is applied (i.e $u = v = w = 0.0$). For Fluent calculations, standard velocity inlet and pressure outlet boundary conditions are used at the inlet and outlet respectively. The inlet velocity profile, turbulence intensity and turbulent length scale are prescribed as above. For walls, a standard no-slip condition and a slip condition with zero shear are used for the lower and upper walls respectively. Full details of the treatment of these boundary conditions may be found in [16].

Calculations are performed on a 2-D mesh consisting of two blocks. Block 1 consists of 166×42 nodes and block 2 has 90×122 nodes. A mesh independence study was performed on a mesh with approximately double the number of grid nodes in each direction. Figure 5 presents (a) horizontal velocity, (b) vertical velocity and (c) cross Reynolds stress profiles at the mid-cavity point where the mesh is coarsest within the cavity. The solution was found to be sufficiently mesh independent for the present comparisons.

The non-dimensional average integral length scales within the cavity shear layer were calculated using Equation (17) and $L_{k-\varepsilon} = k^{3/2}/\varepsilon$ for the standard Menter and $k-\varepsilon$ models respectively. They are compared with the equivalent Poisson-Hamilton-Jacobi length scale. The calculated values were 0.12, 0.1 and 0.46 for the standard Menter, $k-\varepsilon$ and Poisson-Hamilton-Jacobi Menter models respectively. Figure 6 contours phase averaged vorticity from the experimental measurements [23] and the average integral length scales are superimposed. Also included is the phase averaged integral length scale from the LES of Thornber and Drikakis [25] which agrees well with experimental observations. The standard Menter and $k-\varepsilon$ models under predict the nominal length scale in the cavity by 74% and 78% respectively. The length scale calculated

with the Poisson-Hamilton-Jacobi approach, on the other hand, matches the size of the physical vortex in the cavity.

It is reported by Thornber and Drikakis [25] who performed high resolution LES on this case that the physics of the separated cavity shear layer is not significantly sensitive to the level of turbulence applied at the inlet. In the current work, a sensitivity analysis was performed comparing the experimentally measured value of $T_i = 1.5\%$ to a level of $T_i = 5\%$. Figure 7 compares cross Reynolds stress distribution at $x/L = 0.8$ for both the standard and the Poisson-Hamilton-Jacobi Menter models at both levels of turbulence intensity and, as can be seen, low sensitivity is observed.

For profiles where predictions and measurements are compared, percentage errors for velocities and Reynolds stresses are later given. The following experimental data point summations are made:

$$\text{Error}_\phi = \frac{\sum |\phi_{exp} - \phi_{num}|}{\sum |\phi_{exp}|} \qquad (25)$$

where $\phi = u$, v, u'^2, v'^2 or $u'v'$ and the subscripts 'exp' and 'num' represent the experimental measurements and numerical values respectively. For $u'v'$, $\phi_{exp} = u'v'_{exp}$ and $\phi_{num} = u'v'_{num}$. At points where numerical data points do not coincide exactly with measurements, a cubic spline interpolation is used.

Figure 8 shows horizontal velocity profile plots at various locations along the cavity. The $k - \varepsilon$, standard Menter and Poisson-Hamilton-Jacobi Menter models are compared with the experimental LDA measurements of [23]. In addition, the high fidelity LES data of [25] is also included for comparison. Both qualitative a quantitative improvements are observed with the Poisson-Hamilton-Jacobi Menter model. At profile location $x/L = 0.05$ it can be seen that the horizontal velocity component for the standard Menter model is under predicted in the initial shear layer region. The Poisson-Hamilton-Jacobi Menter model, on the other hand, provides an improved prediction which may be partly due to a small re-circulation region observed for the standard Menter model just below the cavity leading edge. Figure 9 (a) shows a streamline plot of this recirculation zone. It acts to retard the flow and extends horizontally to a distance of approximately $\Delta x/L = 0.1$. The $k - \varepsilon$ model performs comparably with the Poisson-Hamilton-Jacobi Menter model at this profile location and no recirculation region is observed. For the standard Menter and $k - \varepsilon$ models, at $x/L = 0.2$, there is insufficient turbulent mixing and the shear layer profile remains sharp. The shear layer growth rate is less accurately captured moving further downstream within the cavity. It is worth noting that the LES fails to accurately capture the shear layer at $x/L = 0.4$ and is less accurate than the Poisson-Hamilton Jacobi method at $x/L = 0.95$. At $x/L = 0.8$ the horizontal velocity component inside the cavity, at $y/L = 2.3$, is significantly under predicted using the standard RANS models and the Poisson-Hamilton-Jacobi Menter model shows a significantly improved trend. Close to the cavity downstream edge, at $x/L = 0.95$, an impingement region was observed. Here, all RANS models predict with a similar level of accuracy. On average, the Poisson-Hamilton-Jacobi Menter model captures the shear layer growth and expansion with greater accuracy than the standard RANS models. Overall, both quantitative and qualitative improvements are observed.

Figure 10 shows a comparison of vertical velocity profiles for the three models. Here, the vertical velocities are approxi-

mately two orders of magnitude lower than the freestream velocity. Table 5 summarizes percentage error variations at different profile locations. At the first profile location ($x/L = 0.05$), close to the cavity leading edge, the Poisson-Hamilton-Jacobi approach shows a significant improvement (59%) over the standard Menter model. This horizontal location corresponds to the recirculation region as shown in Figure 9 (a) and the low value of v, for the standard model, corresponds to the central core of this vortex. As can be seen, this recirculation zone is not predicted by the $k - \varepsilon$ model and hence closer agreement is observed. Interestingly, an improvement is observed using the standard model at $x/L = 0.2$ and the v component for the Poisson-Hamilton-Jacobi model inside the cavity is somewhat under predicted. It should also be noted that the LES fails to predict an accurate trend in this region and the $k - \varepsilon$ model is the least accurate of all. The improvement observed for the standard model is due to a local acceleration of the vertical flow to the right of the separation bubble. At profile location $x/L = 0.8$ there are clear improvements when using the Poisson-Hamilton-Jacobi approach, especially at lower values of y/L inside the cavity. The approach is also considerably more accurate that the LES prediction at this profile location. This is reflected in the tabulated percentage errors with improvements over standard Menter, $k - \varepsilon$ and LES of 32%, 66% and 61% respectively. At $x/L = 0.8$ the standard Menter and $k - \varepsilon$ models show an opposite trend to the measurements. Close to the right-hand cavity wall, the RANS vertical velocity profile trends at $x/L = 0.95$ are similar. The Poisson-Hamilton-Jacobi approach shows improvements over the standard Menter and $k - \varepsilon$ models of 5% and 11% respectively. The LES is approximately 10% more accurate than the Poisson-Hamilton-Jacobi approach. Overall, there are both quantitative and qualitative improvements when using the Poisson-Hamilton-Jacobi model and the evolution of the shear layer is much more accurately captured when compared with the standard RANS models. On average, improvements of 17% and 23% are observed for the vertical velocity profiles when compared with the standard Menter and $k - \varepsilon$ models respectively.

Figure 11 and Table 6 show horizontal Reynolds stress u'^2/U^2 profiles and percentage errors at different profile locations and with the different simulation approaches. As can be seen, the Poisson-Hamilton-Jacobi Menter model shows a significant improvement when compared with the standard RANS models across all profiles. At $x/L = 0.4$, the percentage errors in horizonal Reynolds stress for the standard and $k - \varepsilon$ models are 71% and 81% respectively. The Poisson-Hamilton-Jacobi model on the other hand predicts with an accuracy of 38%. Again, at $x/L = 0.6$, the profile is well predicted by the Poisson-Hamilton-Jacobi Menter model when compared with the $k - \varepsilon$ and standard Menter modelling approaches. At $x/L = 0.8$, all models fail to capture the general trend in the measurements with the exception of the LES, although it should still be noted that on average the Poisson-Hamilton-Jacobi Menter model shows a significant ($\approx 20\%$) improvement over the standard RANS models. It is noted by [23] that the two-dimensional character of the flow is weakened in this region where the mixing layer is subject to strong interaction with the downstream cavity edge. Large scale flow structures generated in the shear layer impinge on the downstream corner and turbulence energy will be created by normal straining (as opposed to shear). It is noted by [23] that the design of the experimental cavity leads to a strong two-dimensional organization of the flow which makes the experimental data adequate for two-dimensional simulations. The Schlieren technique used in the experiments reveals well-defined two dimensional structures. However, it is noted that in the region close to the downstream wall the two-dimensional nature of the flow is weakened. The RANS performs poorly in this region and this is perhaps due to high flow anisotropy and the onset of three-dimensionality. Further RANS model development is likely to be needed to accurately

capture the complex flow physics in this region. This could perhaps be better informed by utilising data from high fidelity CFD simulations such as the LES presented here. Nevertheless, a significant improvement in the average percentage error across all profiles is observed for the Poisson-Hamilton-Jacobi model. Reductions in error of 30% and 38% are observed when compared with the standard Menter and $k - \varepsilon$ RANS models respectively.

Figure 12 shows vertical Reynolds stress v'^2/U^2 at the same profile locations as above. As can be seen, the experimental measurements are significantly different from their horizontal counterpart Reynolds stresses. This is especially so at higher values of x/L where there is complex physical interaction between the vortices and cavity endwall. The predicted profiles for the RANS models on the other hand are almost identical to their horizontal counterparts. This is not surprising given the isotropy inherent in the Boussinesq approximation (i.e. $u' = v' = w'$). Nevertheless, there is a significant improvement through the use of the Poisson-Hamilton-Jacobi Menter model. Table 7 gives average percentage errors and, as can be seen, improvements of 28% and 30% are observed when compared with the standard Menter and $k - \varepsilon$ models respectively. Generally, the LES performs well and is able to account for the increased anisotropy of turbulent velocity fluctuations towards the downstream cavity wall. The peak stress however, at $x/L = 0.8$, is under predicted by around 30%. Figure 13 shows profiles of cross Reynolds stresses. Again significant improvements are observed using the Poisson-Hamilton-Jacobi Menter approach, although the peak shear stress is somewhat under predicted at some locations. At $x/L = 0.8$, results are comparable with the LES prediction. On average, improvements are observed when compared with the standard Menter and $k - \varepsilon$ models of 24% and 28% respectively.

7 CONCLUSIONS

A new turbulence modeling approach is presented that uses Poisson and Hamilton-Jacobi differential equations to set turbulence length scales in cavity flow zones based on expected scales. For complex rim-seal and shroud cavity designs, the method sets an expected length scale based on local cavity width to accurately account for the large-scale wake-like flow structures. The method is tested on three arbitrary complex rim-seal geometries and demonstrates good convergence properties. A smooth transition of the length scale between the cavity and mainstream zones is observed and the Poisson generated length scale provides local fields within the cavity.

The approach is integrated with the popular Menter-SST RANS turbulence model and reduces to the standard Menter model in the mainstream flow. A transonic deep cavity simulation is performed for validation of the model. Overall, the Poisson-Hamilton-Jacobi Menter model shows significant quantitative and qualitative improvements over the standard Menter SST and $k - \varepsilon$ two equation RANS turbulence models. In some instances it is comparable or more accurate than high fidelity LES.

In its current development the approach has been extended through the use of an initial stage of length scale estimation using a Poisson equation and essentially reduces the need for user objectivity. A key aspect of the process is that the length scale is automatically set by the model and not by the modeler. Notably, the current approach is readily implementable in an unstructured, parallel processing computational framework.

The length-scale modification is crude, reflecting the poor predictive accuracy of RANS models for length scales in

separated flows. It is expected that the approach will demonstrate an enhanced capability for more realistic rim-seal and other separated turbomachinery zones. This will be examined as part of future work.

References

[1] Cherry, D., Wadia, A., and Beacock, R., 2005. "Analytical investigation of low pressure turbine with and without endwall gaps seals and clearance features". In ASME Turbo Expo 2005. Paper number GT2005-68492.

[2] Wellbourn, S. R., and Okiishi, T. H., 1998. "The influence of shrouded stator cavity flows on multistage compressor performance". In ASME Turbo Expo 1998. Paper number 98-GT-12.

[3] Rosic, B., Denton, J. D., and Pullan, G., 2005. "The importance of shroud leakage modelling in multistage turbine flow calculations". In ASME Turbo Expo 2005. Paper number GT2005-68459.

[4] Gangwar, A., Lukovic, B., Orkwis, P., and Sekar, B., 2001. "Modelling unsteadiness in steady cavity simulations - part 1: parametic solutions". In Proceedings of the 39th Aerospace Sciences Meeting and Exhibit. Paper number 2001-0153.

[5] Lukovic, B., 2002. "Modeling unsteadiness in steady simulations with neural net- work generated lumped determinstic source terms". PhD Thesis, University of Cincinnati, Department of Aerospace Engineering.

[6] Gangwar, A., 2001. "Source term modeling of rectangular flow cavities". MS Thesis, University of Cincinnati, Department of Aerospace Engineering.

[7] Lukovic, B., Gangwar, A., Orkwis, P., and Sekar, B., 2001. "Modelling unsteadiness in steady cavity simulations - part ii: neural network modelling". In Proceedings of the 39th aerospace sciences meeting an exhibit. Paper number 2001-0154.

[8] Lukovic, B., Orkwis, P., Turner, P., and Sekar, B., 2002. "Effect of cavity l/d variations on neural network-based deterministic unsteadiness source terms". In Proceedings of the 40th aerospace sciences meeting and exhibit. Paper number 2002-0857.

[9] Lukovic, B., Orkwis, P., Turner, P., and Sekar, B., 2002. "Modelling unsteady cavity flows with translating walls". In Proceedings of the 32nd AIAA fluid dynamics conference and exhibit. Paper number 2002-3288.

[10] Jefferson-Loveday, R. J., Tucker, P. G., Northall, J. D., and Rao, V. N., 2013. "Differential equation specification of integral turbulence length scales". *Journal of Turbomachinery,* **135**. 031013.

[11] Fares, E., and Schroder, W., 2002. "A differential equation to determine the wall distance". *International Journal for Numerical Methods in Fluids,* **39**, pp. 743–762.

[12] Spalding, D. B., 1972. "A novel finite difference formulation for differential expressions involving both first and second derivatives". *International Journal for Numerical Methods in Engineering,* **4**, pp. 551–561.

[13] Spalding, D. B., 2013. "Trends, tricks, and try-ons in cfd/cht". *Advances in Heat Transfer,* **45**, pp. 45–47.

[14] Tucker, P. G., and Gaitonde, D. V., 2002. "On the use of higher-order finite-difference schemes on curvilinear and deforming meshes". *Journal of Computational Physics,* **181**, pp. 155–185.

[15] Visbal, M. R., 1998. "Assessment of geometric multilevel convergence and a wall distance method for flows with

multiple internal boundaries". *Applied Mathematical Modelling,* **22**, pp. 293–311.

[16] Ansys Inc., 2013. *ANSYS Fluent Theory Guide*. Ansys, Inc., Canonsburg PA.

[17] Menter, F. R., 1993. "Zonal two equation k ω turbulence models for aerodynamic flows". In Proceedings of the 11th AIAA fluid dynamics conference and exhibit. Paper number 93-2906.

[18] Secundov, N., Strelets, M. K., and Travin, A. K., 2001. "Generalization of $v_t - 92$ turbulence model for shear-free and stagnation point flows". *Journal of Fluids Engineering,* **123**, pp. 111–115.

[19] Strelets, M., 2001. "Detached eddy simulation of massively separated flows". In Proceedings of the 39th AIAA fluid dynamics conference and exhibit. Paper number 2001-0879.

[20] Suponitsky, V., Avital, E., and Gaster, M., 2005. "On three-dimensionality and control of incompressible cavity flow". *Physics of Fluids,* **17**. 104103.

[21] Tyacke, J. C., Tucker, P. G., Jefferson-Loveday, R. J., Rao, V. N., Watson, R., and Naqavi, I., 2013. "Les for turbines: methodologies, cost and future outlooks". In ASME Turbo Expo 2013. Paper number GT2013-94416.

[22] Spalart, P. R., and Allmaras, S. R., 1993. "A one-equation turbulence model for aerodynamic flows". *La Recherche Aerospatiale,* **1**(1), pp. 5–21.

[23] N. Forestier, L. J., and Geffroy, P., 2003. "The mixing layer over a deep cavity at high-subsonic speed". *Journal of Fluid Mechanics,* **475**, pp. 101–144.

[24] Menter, F. R., 1992. "Influence of freestream values on $k - \omega$ turbulence model predictions". *AIAA Journal,* **30**, pp. 1657–1659.

[25] Thornber, B., and Drikakis, D., 2008. "Implicit large-eddy simulation of a deep cavity using high-resolution methods". *AIAA Journal,* **46**, pp. 2634–2645.

8 Tables

Table 1.   Coefficients for filter scheme.

a_0	a_1	a_2
$\frac{5}{8} + \frac{3\alpha_f}{4}$	$\frac{1}{2} + \alpha_f$	$\frac{-1}{8} + \frac{\alpha_f}{4}$

Table 2.   Boundary coefficients for filter scheme at first interior node

a	b	c	d	e
$\frac{1}{16} + \frac{7\alpha_f}{8}$	$\frac{3}{4} + \frac{\alpha_f}{2}$	$\frac{3}{8} + \frac{\alpha_f}{4}$	$-\frac{1}{4} + \frac{\alpha_f}{2}$	$\frac{1}{16} - \frac{\alpha_f}{8}$

Table 3.   Terms and functions of the Menter-SST model

G^k	$-u_i' u_j' (\partial u_i / \partial x_j)$
G^ω	$-(\gamma u_i' u_j' / \nu_T)(\partial u_i / \partial x_j)$
Y^k	$\beta^* \omega k$
Y^ω	$\beta \omega^2$
C^ω	$(2\sigma_{\omega 2}/\omega)(1 - F_1)(\partial k / \partial x_i)(\partial \omega / \partial x_i)$
ν_T	$a_1 k / max(a_1 \omega; \Omega F_2)$
F_1	$tanh\left\{\left\{min\left[max\left(\frac{\sqrt{k}}{\beta^* \omega y}; \frac{500\nu}{y^2 \omega}\right), \frac{4\rho\sigma_{\omega 2}k}{CD_{k\omega}y^2}\right]\right\}^4\right\}$
F_2	$tanh\left[\left[max\left(\frac{2\sqrt{k}}{\beta^* \omega y}; \frac{500\nu}{y^2 \omega}\right)\right]^2\right]$
$CD_{k\omega}$	$max((2\rho\sigma_{\omega 2}/\omega)(\partial k / \partial x_i)(\partial \omega / \partial x_i); 10^{-20})$

Table 4.   Percentage errors in horizontal velocity for the standard Menter model, the Poisson-Hamilton-Jacobi Menter model, the $k - \varepsilon$ model and LES [25].

Model / x/L	0.05	0.2	0.4	0.6	0.8	0.95	Ave
STD Menter	9	6	9	14	19	17	12
PHJ Menter	7	5	7	11	15	14	10
$k - \varepsilon$	7	6	11	18	22	20	14
LES [25]	6	6	6	4	7	17	8

Table 5. Percentage errors in vertical velocity for the standard Menter model, the Poisson-Hamilton-Jacobi Menter model, the $k - \varepsilon$ model and LES [25].

Model / x/L	0.05	0.2	0.4	0.6	0.8	0.95	Ave
STD Menter	94	35	47	84	57	39	59
PHJ Menter	35	51	47	57	25	34	42
$k - \varepsilon$	56	71	65	64	91	45	65
LES [25]	12	27	22	35	86	23	34

Table 6. Percentage errors in horizontal Reynolds stress for the standard Menter model, the Poisson-Hamilton-Jacobi Menter model, the $k - \varepsilon$ model and LES [25].

Model / x/L	0.2	0.4	0.6	0.8	Ave
STD Menter	61	71	77	73	71
PHJ Menter	41	38	38	48	41
$k - \varepsilon$	78	81	80	75	79
LES [25]	33	33	19	18	26

Table 7. Percentage errors in vertical Reynolds stress for the standard Menter model, the Poisson-Hamilton-Jacobi Menter model, the $k - \varepsilon$ model and LES [25].

Model / x/L	0.2	0.4	0.6	0.8	Ave
STD Menter	54	71	80	79	71
PHJ Menter	39	38	47	49	43
$k - \varepsilon$	76	79	83	79	79
LES [25]	43	22	12	24	25

Table 8. Percentage errors in cross Reynolds stress for the standard Menter model, the Poisson-Hamilton-Jacobi Menter model, the $k - \varepsilon$ model and LES [25].

Model / x/L	0.2	0.4	0.6	0.8	Ave
STD Menter	70	83	82	77	78
PHJ Menter	53	57	50	55	54
$k - \varepsilon$	84	85	82	78	82
LES [25]	57	35	28	47	42

9 Figures
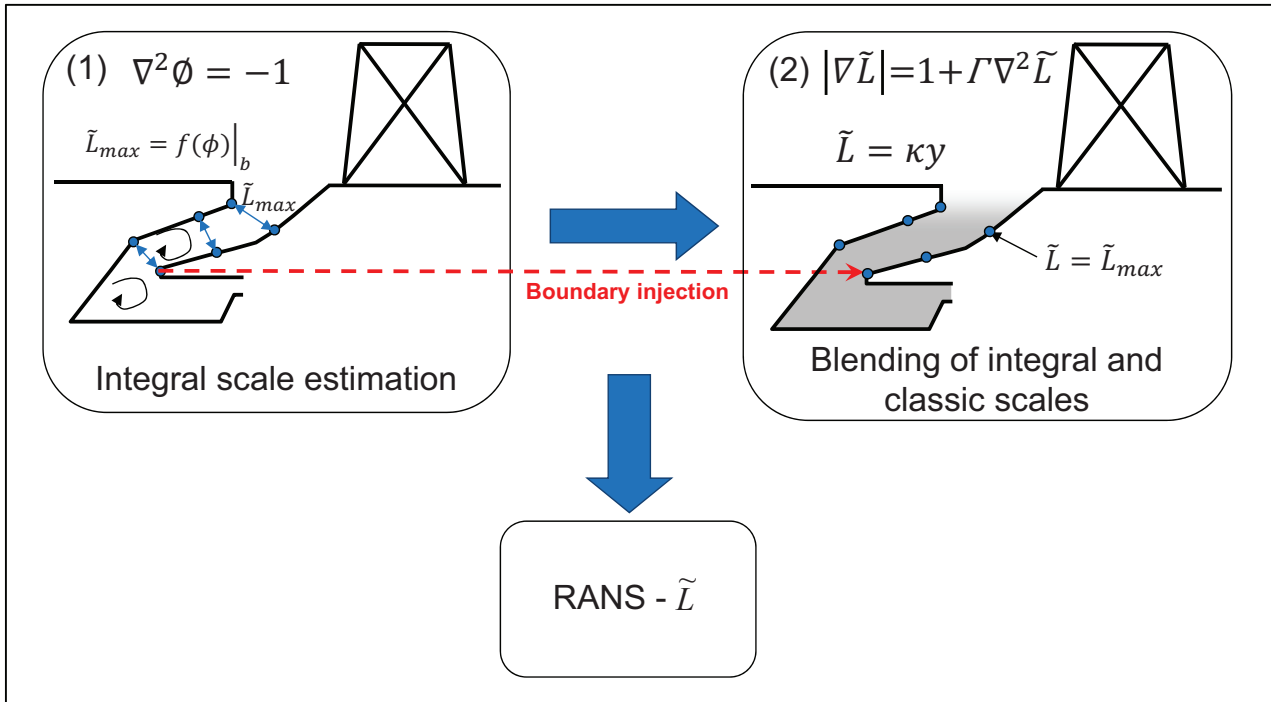
Fig. 1. Process chain for the Poisson-Hamilton-Jacobi length scale method
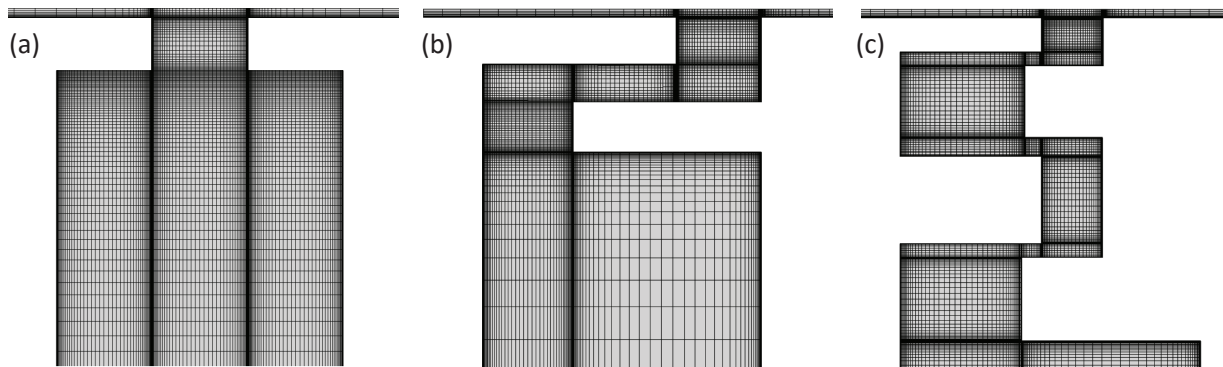
Fig. 2. Computational meshes for: (a) a simple axial seal, (b) a seal with a single radial clearance, (c) a seal with two radial clearances
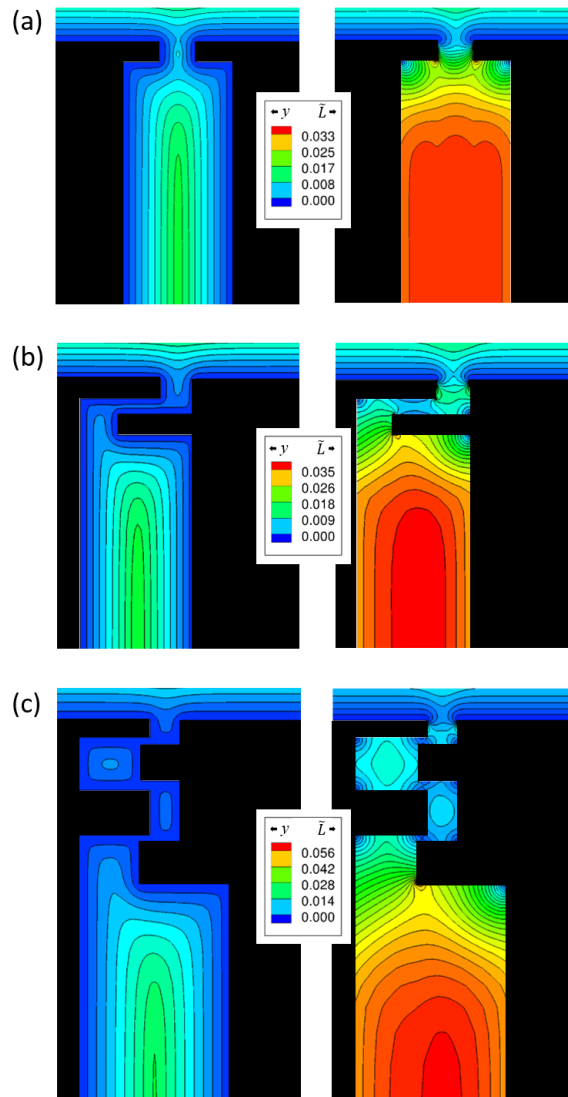
Fig. 3. Left: Contours of standard wall distance y (m), Right: Contours of Poisson-Hamilton-Jacobi length scale $\tilde{L}_{PHJ}$ (m) for: (a) a simple axial seal, (b) a seal with a single radial clearance, (c) a seal with two radial clearances
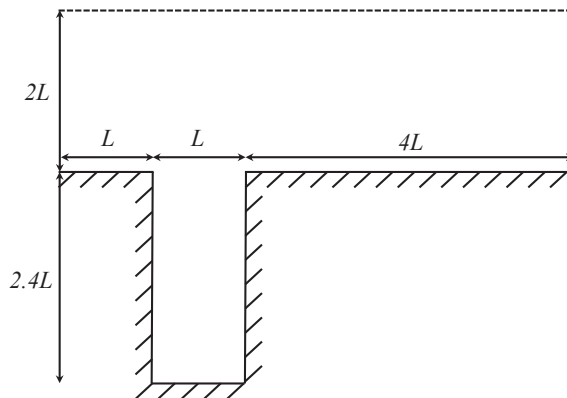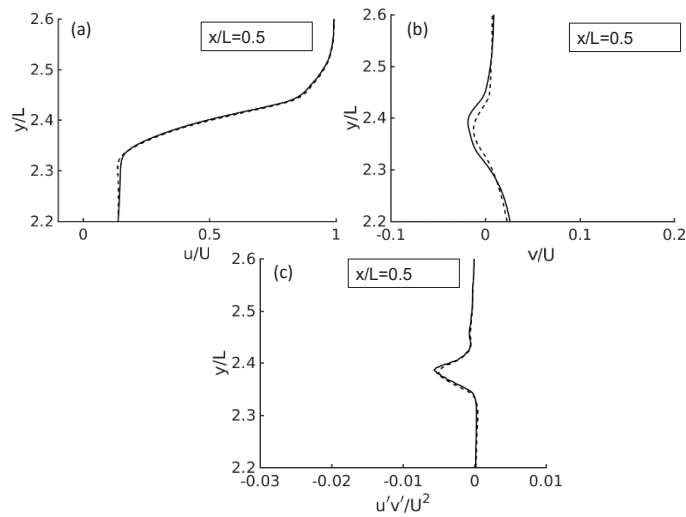

Fig. 4. Schematic of the cavity simulation domain

Fig. 5. Mesh sensitivity for (a) horizontal velocity profile, (b) vertical velocity profile, and (c) cross Reynolds stress at the cavity mid-point $(x/L = 0.5)$
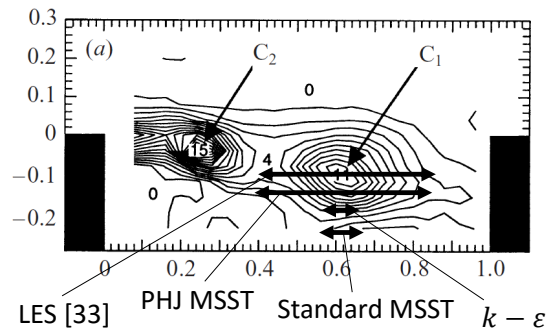
Fig. 6. Experimental vorticity contour plot [23] with the standard Menter, $k - \varepsilon$, Poisson-Hamilton-Jacobi and LES [25] integral length scales superimposed. The centers C_1 and C_2 of the structures are indicated.
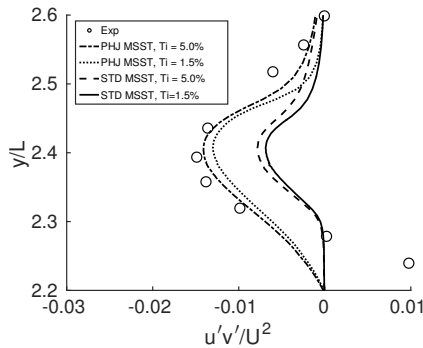
Fig. 7. Cross Reynolds stress sensitivity to inlet turbulent intensity for the standard Menter model $T_i = 1.5\%$ and $T_i = 5.0\%$, Poisson-Hamilton-Jacobi Menter model $T_i = 1.5\%$ and $T_i = 5.0\%$, at location $x/D = 0.8$
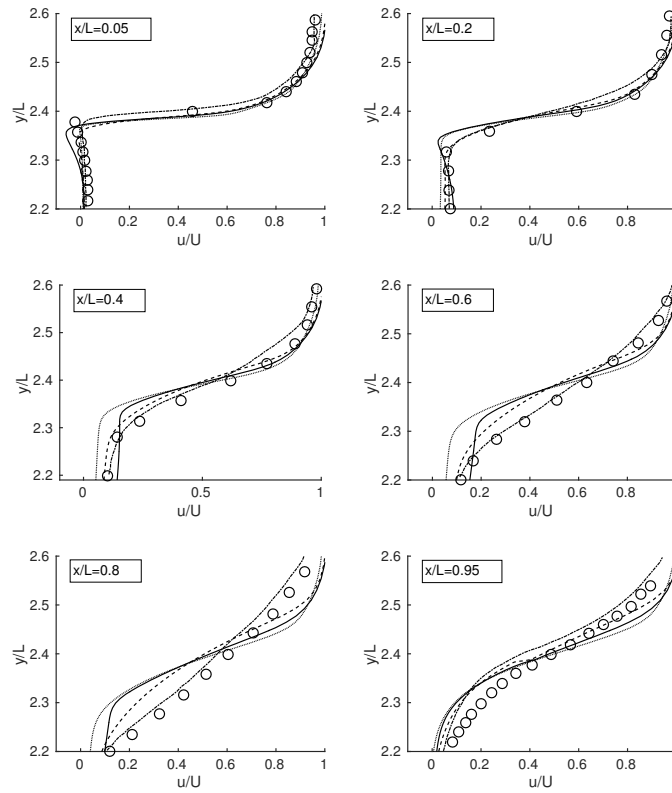
Fig. 8. Comparison horizontal velocity profiles, experimental measurements: $\bigcirc$, standard Menter model: solid curve, $k - \varepsilon$ model: dotted curve, Poisson-Hamilton-Jacobi Menter model: dashed curve, LES [25]: dashed-dotted curve.
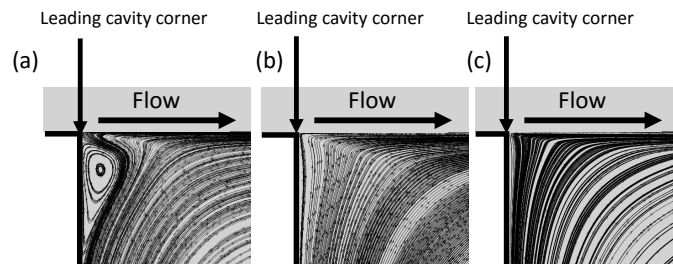

Fig. 9. Flow streamline plots at cavity leading edge, (a) standard Menter model, (b) Poisson-Hamilton-Jacobi Menter model, (c) $k - \varepsilon$ model
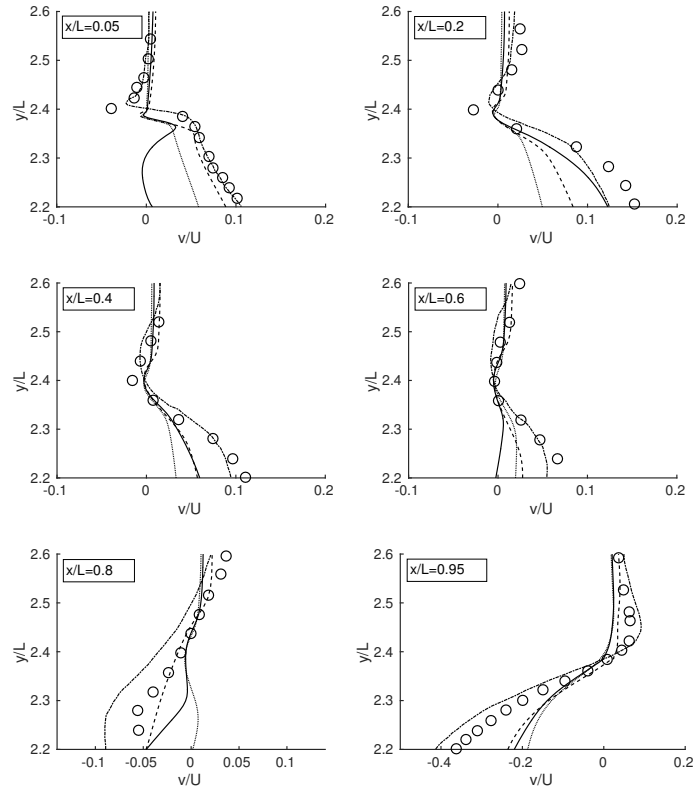
Fig. 10. Comparison vertical velocity profiles, experimental measurements: $\bigcirc$, standard Menter model: solid curve, $k - \varepsilon$ model: dotted curve, Poisson-Hamilton-Jacobi Menter model: dashed curve, LES [25]: dashed-dotted curve.
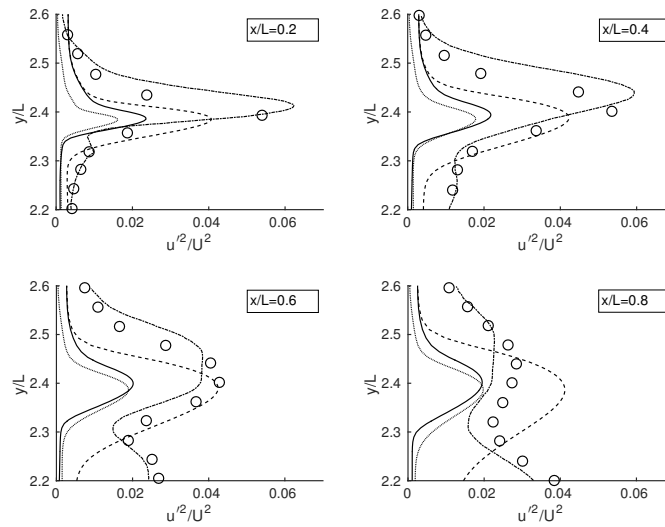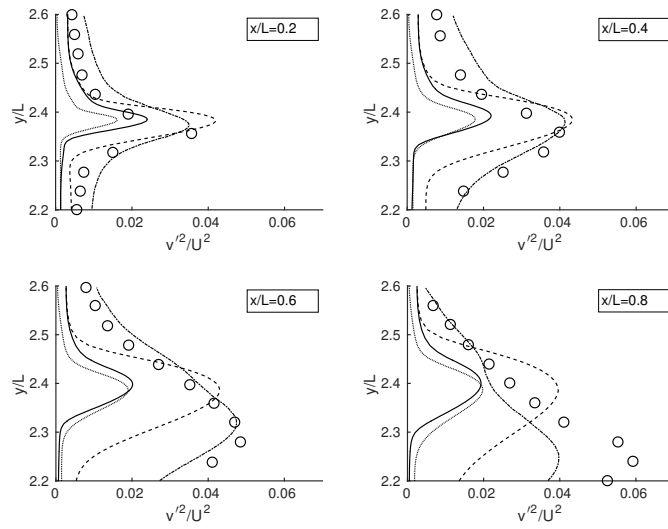

Fig. 11. Comparison horizontal Reynolds stress profiles, experimental measurements: $\bigcirc$, standard Menter model: solid curve, $k - \varepsilon$ model: dotted curve, Poisson-Hamilton-Jacobi Menter model: dashed curve, LES [25]: dashed-dotted curve.

Fig. 12. Comparison vertical Reynolds stress profiles, experimental measurements: ◯, standard Menter model: solid curve, $k - \varepsilon$ model: dotted curve, Poisson-Hamilton-Jacobi Menter model: dashed curve, LES [25]: dashed-dotted curve.
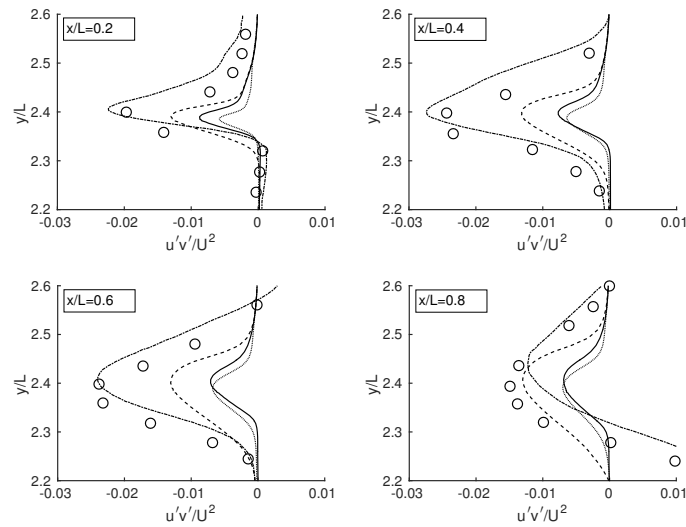

Fig. 13. Comparison cross Reynolds stress profiles, experimental measurements: ◯, standard Menter model: solid curve, $k - \varepsilon$ model: dotted curve, Poisson-Hamilton-Jacobi Menter model: dashed curve, LES [25]: dashed-dotted curve.